Solution processed SnO2:Sb transparent conductive oxide as alternative to Indium Tin Oxide for applications in Organic Light Emitting Diodes

GILLIN, WP

Journal of Materials Chemistry C

Accepted Manuscript

Journal of
Materials Chemistry C

Materials for optical and electronic devices
www.rsc.org/materialsC

Volume 1 | Number 1 | Jan 2013 | Pages 1–100

ROYAL SOCIETY OF CHEMISTRY

ROYAL SOCIETY OF CHEMISTRY

www.rsc.org/materialsC

Journal Name

ARTICLE

Solution processed SnO2:Sb transparent conductive oxide as alternative to Indium Tin Oxide for applications in Organic Light Emitting Diodes

M. Esro,[a] S. Georgakopoulos,[b] H. Lu,[c] G. Vourlias,[d] A. Krier,[e] W. I. Milne,[f] W. P. Gillin[c] and G. Adamopoulos[a*]

Here we present the deposition of antimony-doped tin oxide thin films using the ambient spray pyrolysis technique and demonstrate their implementation as transparent electrodes (anodes) in red, green and blue Organic Light emitting diodes. The films were spray coated at 380 ^{o}C from $SnCl_4$ and $SbCl_3$ solution blends in methanol and ~230 nm thick films were investigated by means of x-ray diffraction, AFM, UV-Vis absorption spectroscopy, 4-point probe, Hall Effect and Kelvin Probe. It was found that for optimum antimony doping in the precursor solution of ~2 wt%, the as-deposited ATO films exhibit excellent characteristics such as low surface roughness of R_{RMS}~6.3 nm, high work function (~ -5.03 eV), wide direct band gap (~4.2 eV), high transparency in the visible spectrum in excess of 85 % on glass, low sheet resistivity (~32 Ohms/sq), high charge carrier concentration (~6.35 × 10^{20} cm^{-3}) and carrier mobility of ~32 cm^2 V^{-1} s^{-1}. Furthermore, the electrical and optical performance i.e. the turn on voltage and external quantum efficiency of red, green and blue OLEDs fabricated on optimized SnO2:Sb films were identical to those of OLEDs fabricated on commercially available ITO (R_s~15 Ohms/sq) and were found to be in excess of 11 %, 0.3 % and 13 % for red, green and blue OLEDs respectively.

Introduction

Transparent electrodes constitute one the most important components in developing a wide range of optoelectronic devices including light-emitting diodes,[1] displays,[2] thin film solar cells,[3] touch screens,[4] and smart windows.[5] Such devices require transparent electrodes that can provide large-area processability and cost-effectiveness combined with high transparency and conductivity. In addition to electrical conductivity and optical transparency, transparent electrodes for thin film optoelectronic devices must be smooth with a suitable work function[6] and surface chemistry,[7] and show stability under bias stress.

Moreover, the rapidly growing demand for consumer electronics, smart building materials and photovoltaics, requires the development of lower cost but equally high performance TCOs both in terms of conductivity and transparency.

Currently, and over the last four decades, indium tin oxide (ITO) is the most commonly used transparent electrode material and has demonstrated with excellent conductivity and optical transparency.[8,9] Despite the fact that ITO still constitutes the material of choice it is rather undesirable for large-area, low-cost applications due to the scarcity of indium and its expensive vacuum deposition based fabrication methods. As an alternative route, a wide range of emerging alternatives have been investigated. Those include single-walled carbon nanotubes,[10-14] silver nanowires,[4,15-18] conjugated polymers,[19,20] graphenes[21-24] and hybrids of these.[25,26] Based on the latter materials, transparent conducting electrodes with performance comparable to that of ITO have been produced and functional devices have been demonstrated.[27-30] However, the optical transparency of these nonoxide-based electrodes highly depends on the film thickness and the development of fabrication processes in order to provide homogeneous and very thin films over large is challenging especially for industrial applications. To that end further efforts have been focused on the investigation of TCOs mainly based on zinc oxide (ZnO)[9] and tin oxide (SnO2) employing a wide range of deposition techniques. Amongst these, tin oxide (SnO2) is a well-investigated transparent semiconductor with a large band gap in the range between 3.5 and 4.1 eV[31-33] high transparency in the visible range and high n-type electric conductivity,[34] which makes it a promising alternative to ITO. Tin oxide's electrical properties have been further improved by incorporation of numerous doping elements such as W,[35] In,[36] Pb,[37] V,[38] and Sb.[39,40] Antimony-doped SnO2 in particular constitutes a promising candidate as it exhibits quasimetallic conductivity maintaining at the same time its transparency in the visible range.[41]

a. *Engineering Department, Lancaster University, Lancaster LA1 4YR, UK.*
b. *Institut de Ciència de Materials de Barcelona, Campus de la Universitat Autónoma de Barcelona, 08193 Bellaterra, SPAIN.*
c. *Materials Research Institute, and School of Physics and Astronomy, Queen Mary University of London, Mile End Road, London, E1 4NS, UK.*
d. *Physics Department, Aristotle University of Thessaloniki, Thessaloniki 54142, GREECE.*
e. Quantum Technology Centre, Department of Physics, University of Lancaster, LA1 4YB, UK.
f. Department of Engineering, University of Cambridge, 9 JJ Thomson Avenue Cambridge CB3 0FA, UK.
* E-mail: g.adamopoulos@lancaster.ac.uk

ARTICLE

SnO_2:Sb films have also been deposited using a wide range of deposition techniques namely the magnetron sputtering,[42,43] e-beam evaporation,[44] Atomic Layer Deposition,[45] chemical vapor deposition,[46] DC glow discharge,[47] molecular beam epitaxy,[48] spray pyrolysis,[49,50] sol-gel,[51,52] and more recently spin cast from preformed SnO_2:Sb nanocrystals.[52-54]

Amongst the wide range of deposition techniques, a solution-based method could provide a variety of appealing advantages such as simplicity, low cost, and high throughput. Unlike, the sol–gel method that typically produces amorphous films that require post deposition annealing at high temperatures to induce crystallization, a process that often affects the quality of the films through the formation of cracks, phase segregation in the case of doped metal oxides and increased surface roughness, spray pyrolysis constitutes an attractive alternative that has been used as a technique for glass coating. This technique however often resulted in irregular surfaces, a limiting factor for the films implementation in thin film device electrodes. Meanwhile, the deposition of smooth and highly conducting SnO_2:Sb film as alternative to ITO and its it use as a functional thin film transistor gate electrode has recently been demonstrated.[55]

This work reports on the application of ambient spray pyrolysis for the deposition of highly transparent, high work function SnO_2:Sb thin films and their implementation as anodes in Organic Light Emitting Diodes (OLED). In particular the optical, structural, surface and electrical properties of the films are being investigated and assessed as a function of the Sb content.

Experimental

Materials and methods

SnO_2:Sb, deposition by Spray Pyrolysis: A 20 mg/ml precursor solution of tin chloride ($SnCl_4$) and 5 mg/ml of antimony chloride ($SbCl_3$) was prepared in methanol. Sb doping $[Sb^{3+}]/[Sn^{4+}+ Sb^{3+}]$ wt% was achieved by blending the tin chloride solution with the desired quantity of the antimony chloride solution. Corning 1737 glass substrates were kept at 380 ^{o}C on a hotplate, while aerosols of the blend were sprayed onto the substrate employing a pneumatic airbrush, held at a vertical distance of about 20 cm. After a period of 5 s, the spraying process was interrupted for 10 s to allow for the vapors to settle onto the sample before the cycle was repeated until films of typical thicknesses of 220 nm were obtained.

UV–Vis Absorption Spectroscopy: The optical transmission spectra of SnO_2:Sb films on fused silica and glass substrates were measured at wavelengths between 175 nm and 2500 nm using an Agilent Cary 5000 spectrometer.

Atomic Force Microscopy: Atomic force microscopy images were taken in tapping mode under ambient conditions using a Veeco Dimension 3100 SPM system using a silicon tip of a radius < 10 nm.

Kelvin Probe: The work function of SnO_2:Sb films was determined using an ambient Kelvin probe system (KP Technology Ltd) employing a gold tip with a diameter of 0.1 mm over a scanning area of 10 x 10 mm.

Electrical properties: The sheet resistivities of the SnO_2:Sb films were measured at room temperature by applying the four-terminal sensing technique using a Jandel Multi Height Probe system with an Agilent B1500A semiconductor parameter analyzer. The films were investigated further by applying the Van der Pauw method (film size 10 x 10 mm) on a Hall Effect measurement system with a 0.5 T magnet kit.

X-ray Diffraction: The X-ray diffraction patterns of SnO_2:Sb films on glass were measured in the grazing incidence mode geometry (GIXRD) using a Rigaku Ultima+ diffractometer with CuKα radiation operating at 40 kV and 30 mA. The crystal size, was estimated from diffraction line broadening using Scherrer's formula (broadening factor ~0.9).

Spectroscopic ellipsometry: SE measurements of SnO_2:Sb films on intrinsic Si were studied with ex situ UV–visible spectroscopic ellipsometry in the range of photon energies from 1.5 to 6 eV in steps of 20 meV at an incidence angle of 70° using a Jobin Yvon UVISEL phase modulated system. Parameterization of optical constants in the UV–visible range was based on the fact that the energy dependent dielectric function ε(E) of a semiconductor can be expressed by the contributions of band-to-band optical transitions that can be taken into account by Lorentzian and Drude oscillators. In the present study, two Lorentz oscillators were found to yield a good fit to the data and were consistent with the electronic structure i.e. one oscillator that models the fundamental optical transitions and another in the UV range that takes into account contributions from higher band-to-band transitions.

OLED fabrication: Initially, all organic materials were purified by vacuum sublimation prior to use. All the layers were deposited in a high-vacuum (10^{-7} mbar) Kurt J. Lesker thermal evaporation system onto SnO_2:Sb and commercially available ITO (R_s: 15 Ohms/sq) coated glass substrates using typical deposition rates of 0.1 nm s^{-1} to 0.3 nm s^{-1}. The thickness of each layer was measured by an in-situ quartz crystal monitor and independently confirmed by ellipsometry and profilometry. For ITO substrates only, oxygen plasma treatment was performed in a Diener Electronic Femto plasma system before organic deposition. The following section describes the structures of the Red, Green and Blue OLEDs used in this work.[56-61]

Red OLED structure: A 15 nm layer of N,N'-Di(1-naphthyl)-N,N'-diphenyl-(1,1'-biphenyl)-4,4'-diamine (NPB) was used as the hole injection layer followed by a 20 nm tris(4-carbazoyl-9-ylphenyl)amine (TCTA) hole transporting layer. The light emitting layer with a thickness of about 30 nm consisted of 9,9'-(4,4'-(phenylphosphoryl) bis-(4,1-phenylene))bis(9H-carbazole) (BCPO) doped (7 wt%) with tris[1-phenylisoquinoline-C2,N]iridium(III) (Ir(piq)3). The structure was completed by a 10 nm thick 2,9-Dimethyl-4,7-diphenyl-1,10-phenanthroline, (BCP) electron transporting layer, and a 45 nm tris-(8-hydroxyquinoline)aluminium (Alq3) electron injection layer. The cathode comprised of a 1 nm LiF followed by the thermal evaporation of 100 nm Al.

Green OLED structure: A rather simple device structure was adopted for the green OLED that consists of a 50 nm N,N'-Bis(3-methylphenyl)-N,N'-bis(phenyl)benzidine (TPD) hole injection layer,

a 50 nm thick light emitting layer of tris-(8-hydroxyquinoline) aluminium (Alq3) and LiF (1 nm)/Al(100 nm) layers as anodes.

Blue OLED structure: A 30 nm layer of N,N'-Di(1-naphthyl)-N,N'-diphenyl-(1,1'-biphenyl)-4,4'-diamine (NPB) was used as the hole injection layer followed by a 20 nm thick 1,3-bis(N-carbazolyl)benzene (mCP) hole transporting layer (also an exciton blocker). The light emitting layer of a thickness of 25 nm was consisted of 9,9'-(4,4'-(phenylphosphoryl) bis-(4,1-phenylene)) bis(9H-carbazole) (BCPO) doped (8 wt%) with bis[2-(4,6-difluorophenyl)pyridinato-C2,N](picolinato)iridium(III) (FIrpic). A 3-(biphenyl-4-yl)-5-(4-tert-butylphenyl)-4-phenyl-4H-1,2,4-triazole (TAZ) 50 nm thick layer served as the electron transporting layer electron transporting layer and the device was completed by the cathode that was consisting of a 1 nm LiF and 100 nm Al.

OLED characterization: The devices were characterized in a nitrogen atmosphere using an integrating sphere with a calibrated silicon photodetector (Newport 818-SL). Voltage sourcing and current measurements were performed using a Keithley 236 source-measure unit and the optical power output was measured using a Newport 1830 optical power meter.

Results and discussion

The UV–vis transmission spectra of ~50 nm thick SnO$_2$:Sb films deposited on fused silica substrates with varying the [Sb^{3+}]/[Sb^{3+}+Sn^{4+}] (wt%) ratio are illustrated in Figure 1a. The Tauc plots[62] that show the onset of the optical transitions near the band edge of key SnO$_2$:Sb films (for clarity) are also depicted in Figure 1b and indicate that the direct transition is the dominant transition involved.
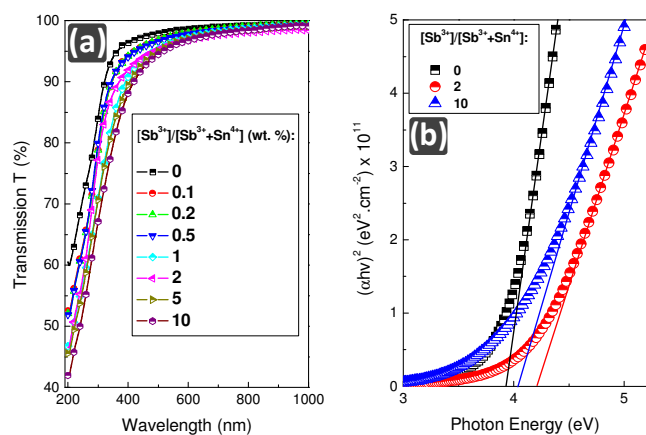

Figure 1: a) UV-Vis transmission (%) spectra and **b)** Tauc plots of selected SnO$_2$:Sb films on fused silica as a function of the [Sb^{+3}]/[Sb^{+3}+Sn^{+4}] (wt%) ratio (in the solution).

The variation of the optical band gap as well as the Urbach tail energy of SnO$_2$:Sb films with different Sb doping levels are shown in Figures 2a and 2b respectively. Note, that for SnO$_2$ with several optical and acoustical modes the presence of an indirect transition has been reported however, the calculated band structure for pure

SnO$_2$ (as well as the data in the present study) do not indicate the presence of any lower indirect gap.[31,41]

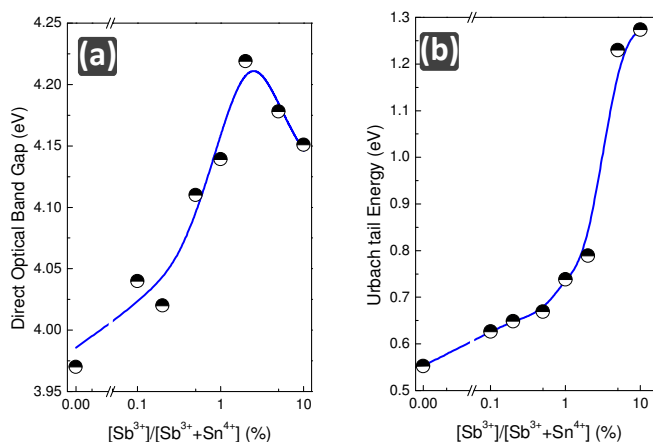**Figure 2: a)** Direct optical band gap **b)** Urbach tail energy of SnO$_2$:Sb films on used silica as a function of the [Sb^{+3}]/[Sb^{+3}+Sn^{+4}] (wt%) ratio (in the solution). The solid lines are guide to the eye.

From Figure 2a, it is seen that the fundamental absorption edge of the SnO$_2$:Sb films shifts up from ~3.97 eV to ~4.22 eV with the increase of the Sb content showing a maximum for an Sb content of 2 wt%. For Sb concentrations in excess of 2 wt% the optical band gap decreases whereas the Urbach tail energy increases monotonically along with the [Sb^{+3}]/[Sb^{+3}+Sn^{+4}] (wt%) ratio in the range between 0 and 10 %. Also and as will be discussed later, the dependence of the overall transparency of thicker SnO$_2$:Sb films on glass shows the same trend as that of the optical band gap also reaching its maximum for an Sb content of 2 wt%.

To interpret further the optical data, van der Pauw's technique was employed to measure the electrical properties of the films. The SnO$_2$:Sb films (220 – 230 nm thick on glass) sheet resistivity, resistivity, charge carrier concentration and charge carrier mobility as a function of the Sb content are depicted in Figures 3a, 3b, 3c and 3d respectively.

The results depicted in Figure 3 clearly indicate controllable electron doping of SnO$_2$ using Sb. More precisely, the electron concentration, n, increased from 4.25 × 10^{19} to 6.35 × 10^{20} cm^{-3} while the [Sb^{+3}]/[Sb^{+3}+Sn^{+4}] (wt%) concentration ranged between 0 and 2 %. The electron mobility μ_e, showed the same trend reaching a maximum of ~32 cm^2 V^{-1} s^{-1} for an Sb concentration of 2 %. Equally, the corresponding resistivity ρ, and sheet resistivity R$_s$ reached their minimum values of 7.35 × 10^{-4} Ohms cm and 32 Ohms/sq respectively. As the Sb content increased further, the electron mobility and charge carrier concentration decreased from 32 to 3.4 cm^2 V^{-1} s^{-1} and 6.35 × 10^{20} to 2.7 × 10^{20} cm^{-3} respectively. In parallel, the corresponding resistivity and sheet resistivity showed a rather steep increase for higher Sb doping.

The shift in the fundamental absorption edge from 3.97 eV to 4.22 eV along with the respective increase of the carrier concentration from 4.25 × 10^{19} to 6.35 × 10^{20} cm^{-3} for Sb doping levels between 0

ARTICLE

Journal Name

and 2 wt% may be attributed to the Moss-Burstein shift,[63] which occurs due to filling up of low lying energy levels by the conduction electrons.
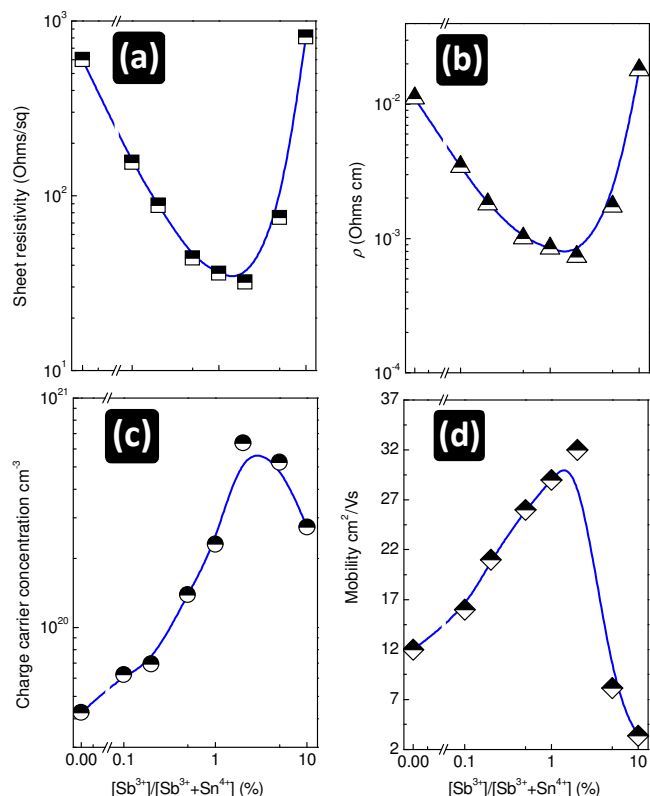

Figure 3: a) Sheet resistivity, **b)** resistivity, **c)** carrier concentration and **d)** electron mobility of SnO$_2$:Sb films on glass as a function of the [Sb^{+3}]/[Sb^{+3}+Sn^{+4}] (wt%) ratio (in the solution). The solid lines are guide to the eye.

Such an upshift in the absorption edge with Sb doping is consistent with previous findings and can be attributed to the non-parabolicity of the bands near the center of the Brillouin zone and consequently to the variation in effective mass of electrons in the conduction band.[64] Moreover, the increase in carrier concentration with increase of the Sb doping concentration is due to the fact that Sb (Sb^{+5} in particular) forms a shallow donor level close to the conduction band of SnO$_2$.[65] The decrease however of the carrier concentration for Sb doping in excess of 2% is probably due to increased disorder that results from an increase in the activation energy of the donor.[65] The latter is consistent with the monotonic increase of the Urbach tail energy (Figure 2b) with increasing the Sb content and the steep increase in particular for Sb doping in excess of 2 %, as such an increase of the Urbach tail energy denotes increase of the density of defect states, perturbation of the parabolic density of states at the band edge, loss of stoichiometry or change of the valence state of the doping element. The latter in particular is further supported by the variation of the SnO$_2$:Sb films (~230 nm on fused silica) average transparency in the visible spectrum (400 nm – 700 nm) that is shown is Figure 4a. In Figure 4b, the transmittance (%) of an ITO reference sample (R$_s$~15 Ohms)

as well as a SnO$_2$:Sb(2%) film (~230nm) on glass are illustrated. Based on the reported average transmittances of both the SnO$_2$:Sb(2 wt%) and commercially available ITO in the visible range (inset Figure 4b) the Haacke figure of merit[66] was found to be ~6.37 10^{-3} Ω^{-1} and ~13.59 10^{-3} Ω^{-1} for SnO$_2$:Sb(2%) and ITO respectively.
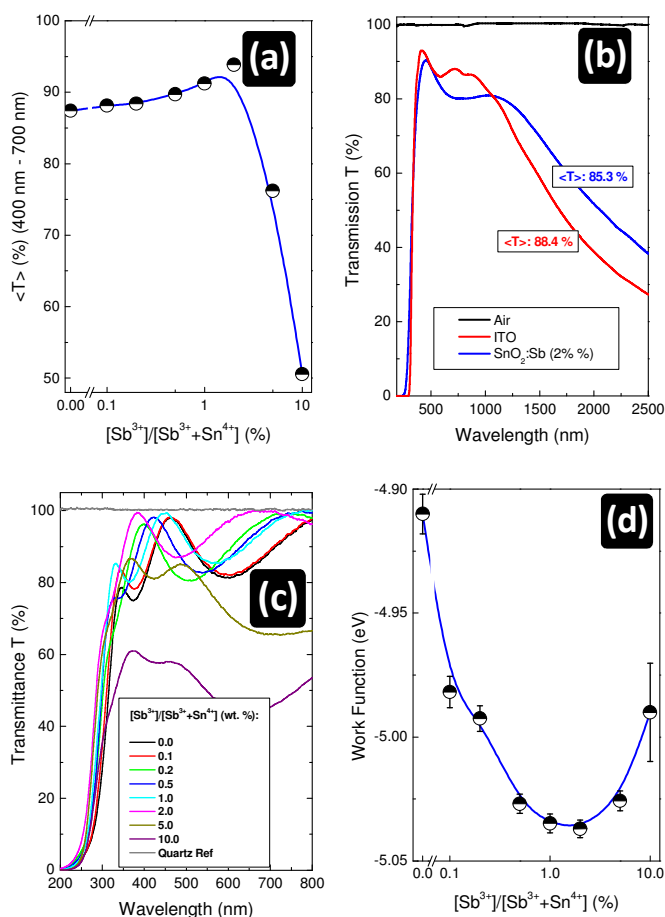
Figure 4: a) Average transmittance in the visible spectrum of SnO$_2$:Sb films on fused silica as a function of the [Sb^{+3}]/[Sb^{+3}+Sn^{+4}] (wt%) ratio (in the solution). **b)** Transmittance % of ITO and SnO$_2$:Sb (2 wt%) on glass. **c)** UV-Vis transmission spectra of SnO$_2$:Sb films on fused silica. d) Work function of SnO$_2$:Sb films (~230 nm) on glass as a function of the [Sb^{+3}]/[Sb^{+3}+Sn^{+4}] (wt%) ratio (in the solution). The solid lines are guide to the eye.

The increase in the films transparency with increase of the Sb incorporation up to 2 % has been attributed to the substitutional doping by pentavalent antimony Sb^{5+}. For increased Sb doping levels in excess of 2 % the increase of the films' opacity has been attributed to substitutional doping by trivalent antimony Sb^{3+}.[67]

In practical applications, (organic light emitting diodes in particular), the alignment of the work function of the anode material with respect to the highest occupied molecular orbital (HOMO) levels of a typical hole transport layer, constitutes a major issue. To that end, alternative materials to ITO have been investigated as anodes.[68,69] However, the vast majority suffer from some combination of lower work functions than ITO or poor optical transparency, although high work function TCOs have been reported.[7] The work function of

SnO_2:Sb films as a function of the Sb content is depicted in Figure 4d. The work function of the ITO reference was measured as -4.75 eV and -4.93 eV before and after O_2 plasma treatment respectively.

Although the underlying mechanism is not quite clear, the work function changes may be attributed to changes in surface termination or surface orientation[70-72] perhaps due to the removal of bridging and in-plane oxygen atoms[72] by the incorporation of Sb^{+5}. Additionally, the change of the work function may be attributed to the change of the material's crystallographic orientation from (200) to (110)[73] which is the case in this work as shown in Figure 5 where the (normalized - to the (200) peak height) SnO_2:Sb patterns as a function of the Sb doping incorporation are illustrated.
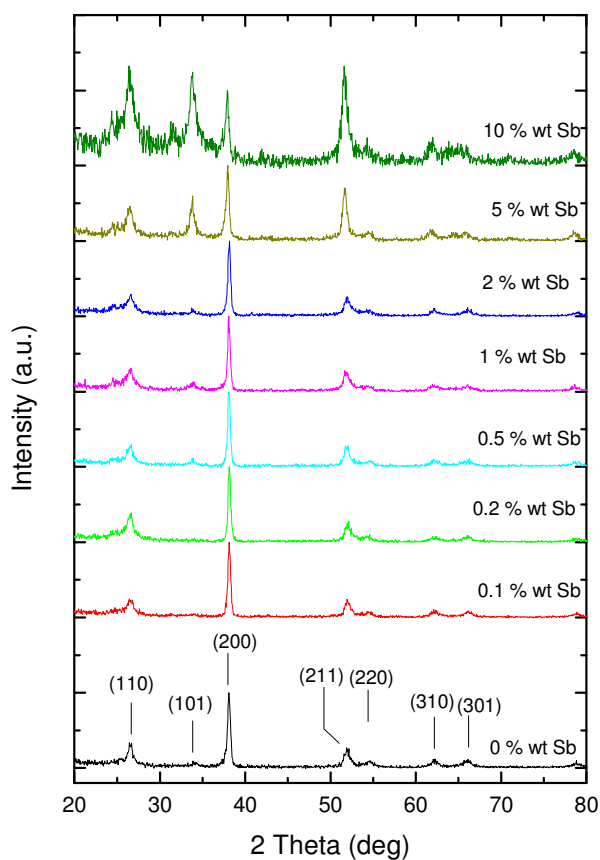

Figure 5: GIXRD patterns of SnO_2:Sb with different $[Sb^{+3}]/[Sb^{+3}+Sn^{+4}]$ (wt%) ratio (in the solution). The patterns were normalized to the (200) peak height.

The XRD patterns of the SnO_2:Sb films contain diffraction lines characteristic of cassiterite ($P4_2/mnm$, ICDD 41-1445) including those with an antimony content up to 10 wt%. Moreover, the presence of a single crystalline phase (related to cassiterite), indicates that the SnO_2 lattice can accommodate at least up 10 wt% Sb atoms without significant changes in the structure. The patterns analysis results based on a $P4_2/mnm$ tetragonal crystal structure are summarized in Figure 6.
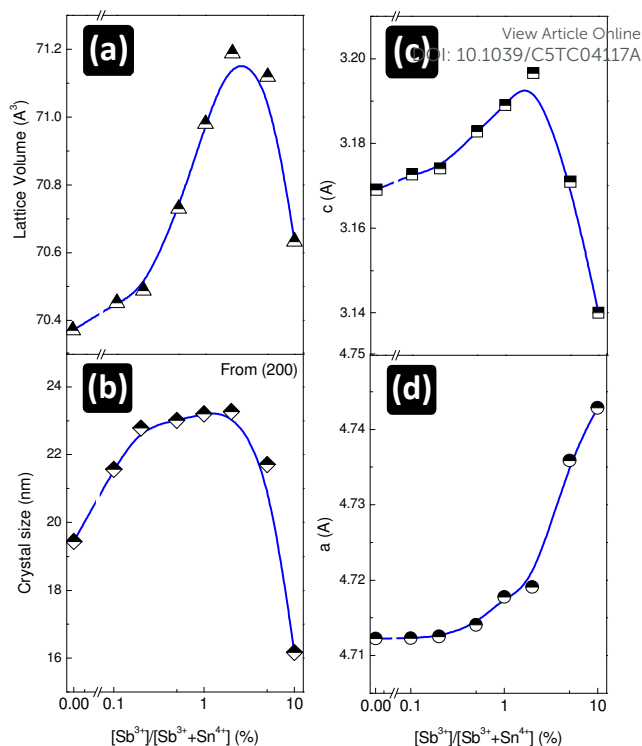

Figure 6: a) Lattice volume, **b)** average crystal size, **c)** c and **d)** a unit cell parameters of SnO_2:Sb films as a function of the $[Sb^{+3}]/[Sb^{+3}+Sn^{+4}]$ (wt%) ratio (in the solution). The solid lines are guide to the eye.

One can immediately observe the broadening of the SnO_2:Sb for Sb content in excess of 2 % denoting the decrease of the crystal size, an observation that is further supported by Figure 6b. Evidently, Sb incorporation also results in a change in the growth orientation along the (110) and (101) planes. Additionally, Figures 6a and 6b show that the a-axis length increases monotonically with increase of the Sb content perhaps due to the segregation of Sb to the surface of the particles. This is also consistent with the depression of the crystalline growth of films with high Sb content. On the other hand, both the c-axis length along with the average crystal size and the lattice volume reach a maximum at a Sb content of 2 wt%.

As the scattering at grain boundaries is the dominant scattering mechanism that limits the mobility in polycrystalline materials, the surface roughness constitutes an important factor for the implementation of the films in devices. Therefore, the SnO_2:Sb films were further characterized by AFM. Topography images of selected SnO_2:Sb (~230 nm) films on glass with different Sb content as depicted in Figure 7 clearly illustrate films of low surface roughness of about 6 nm (rms) for SnO_2:Sb films deposited at optimum conditions i.e. $[Sb^{+3}]/[Sb^{+3}+Sn^{+4}]$ ratio of 2. The images presented are the topography images after they have been flattened out (z-offset adjustment). Further image processing (e.g. for tip dilation) was omitted as it showed no effect on the image quality. The surface roughness of the ITO reference film was found to be of ~3.2 nm (rms). It is clearly seen from Figure 8 that the SnO_2:Sb films are nanocrystalline having uniformly distributed crystallites. The grain size of the SnO_2:Sb films was found to increase with Sb incorporation however the images show no further trends with the

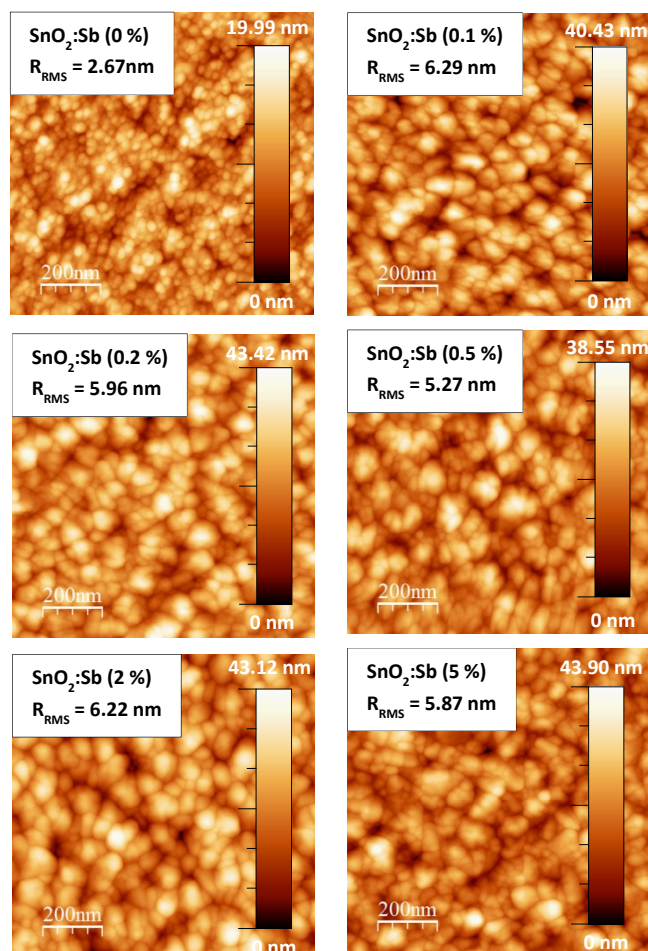Sb content. More importantly, what should be noticed is the films' excellent uniformity and the absence of pinholes.

Figure 7: AFM topography images (RMS roughness inset) of solution processed $SnO_2:Sb$ films on glass for different $[Sb^{+3}]/[Sb^{+3}+Sn^{+4}]$ (wt%) ratio (in the solution).

In order to demonstrate the potential of spray coated $SnO_2:Sb$ films (~230 nm) grown under optimum conditions (in terms of the Sb content) for use as transparent electrodes, we have implemented them as anodes in red, green and blue OLEDs employing well-established device architectures as described in the experimental section. Representative current density, light power and external quantum efficiency plots for all the red, green and blue OLEDs are shown in Figure 8.

Figure 8 reveals small differences in terms of the voltage-current density characteristics and emitted light power for OLEDs fabricated on commercially available ITO (R_s~15 Ohms/sq) and spray coated $SnO_2:Sb$ anodes (grown at optimum conditions i.e. $[Sb^{+3}]/[Sb^{+3}+Sn^{+4}]$ ratio of 2 in the solution) whereas Figure 10 illustrates the band alignment of SnO2:Sb, ITO and organic stacks. On the other hand, all OLEDs using commercially available ITO (R_s~15 Ohms/) show identical turn-on voltages and external quantum efficiencies with those that implement spray coated $SnO_2:Sb$ (2 wt%.) anodes, reaching high values in excess of 11, 0.3, and 13 % for Red, Green and Blue respectively.
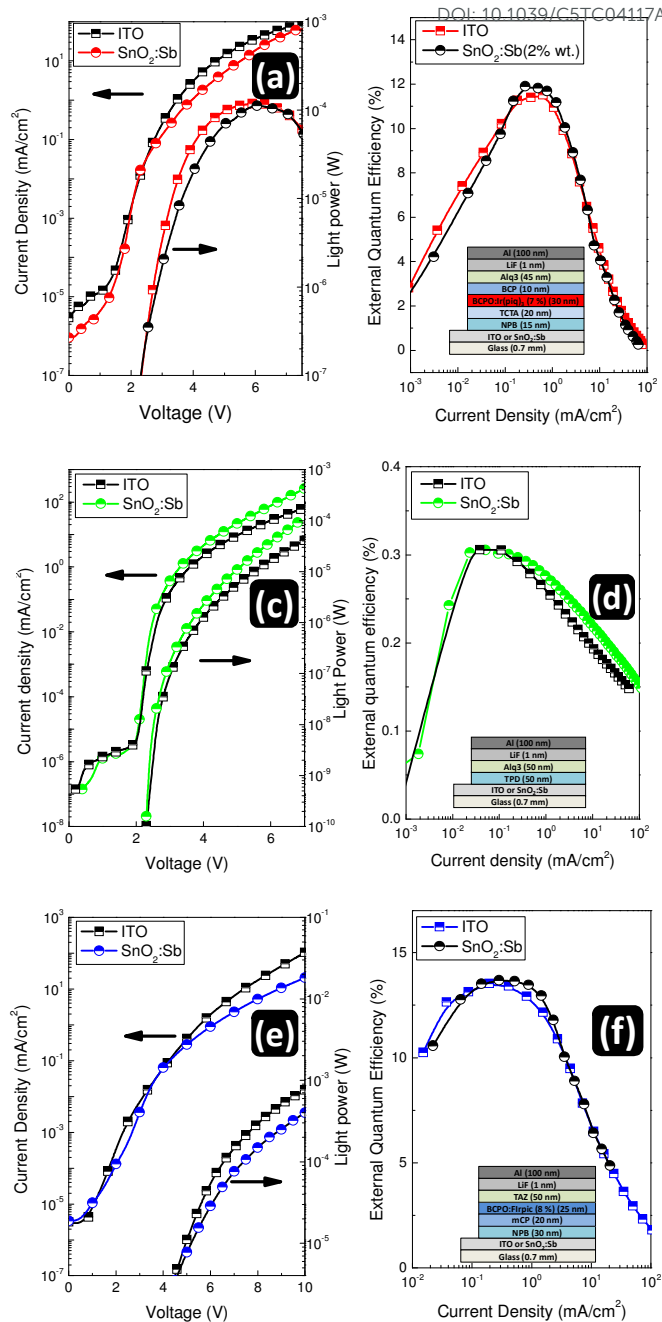

Figure 8: Current density, light power and external quantum efficiency of ITO and $SnO_2:Sb$ (2 wt% in solution) based red **(a, b)**, green **(c, d)** and blue **(e, f)** OLEDs.
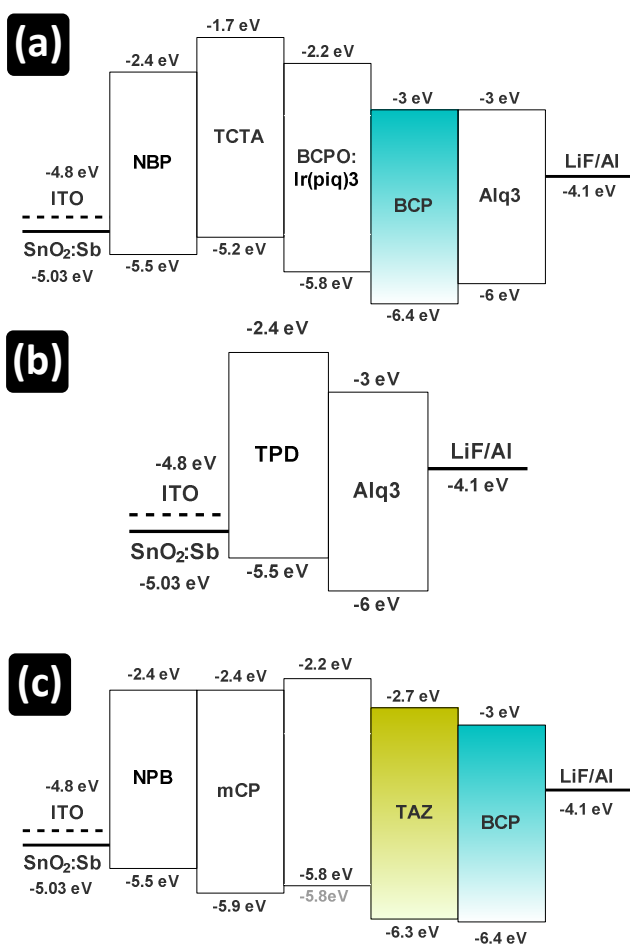
Figure 9: Energy band diagrams of SnO_2:Sb and ITO and organic materials used for **a)** red, **b)** green and c) blue organic light emitting diodes.

Conclusion

This work reported on the deposition and characterization of SnO_2:Sb films as a function of the Sb content and their implementation in Red, Green and Blue OLEDs. It was found that films that were grown using optimized precursor solution blends with Sb content of ~2 wt% show excellent optical and electronic transport properties i.e. wide band gap of ~4.2 eV, high transparency in the visible spectrum of ~93.8 % and ~85.3 % on fused silica and glass substrates respectively (film thickness of ~230 nm), low sheet resistivity of ~32 Ohms/sq, high charge carrier concentration (~6.35×10^{20} cm^{-3}) and electron mobility (~32 cm^2 V^{-1} s^{-1}) and significantly improved (compared to ITO, -4.7 eV) work function of ~ -5.03 eV. Further investigation also revealed smooth films (R_{RMS}~6.3 nm) of a cassiterite-related structure over the reported Sb doping range that showed increased lattice volume for optimal Sb doping of the precursor solution of 2 wt%. SnO_2:Sb films with optimal Sb doping level of 2 wt% (in the precursor solution) as well as commercially available ITO (R_s~15 Ohms/sq) were implemented as anodes in red, green and blue OLEDs. It was found that the electrical and optical performance of the OLEDs fabricated on optimized SnO_2:Sb films was comparable to that of the OLEDs fabricated on the ITO film.

The findings of this work expand the possibilities for ITO replacement for applications in OLEDs using SnO_2:Sb (2 wt%) that can be readily processed onto large area substrates using a spray pyrolysis technique which is a rather simple and low cost deposition process. A remarkable aspect of this approach was the accurate control over the electronic and optical properties of the spray deposited films through simple physical blending of precursor solutions and soluble dopant molecules that clearly demonstrate the potential for the rapid development and implementation of TCOs other than ITO beyond those accessible by traditional deposition methods.

Acknowledgements

Notes and references

1   V. Wood, M. J. Panzer, J. E. Halpert, J. M. Caruge, M. G. Bawendi, V. Bulović, ACS Nano 2009, **3**, 3581.
2   C. Hilsum, Philos. Trans. A. Math. Phys. Eng. Sci. 2010, **368**, 1027.
3   A. G. Pattantyus-Abraham, I. J. Kramer, A. R. Barkhouse, X. Wang, G. Konstantatos, R. Debnath, L. Levina, I. Raabe, M. K. Nazeeruddin, M. Grätzel, E. H. Sargent, ACS Nano 2010, **4**, 3374.
4   M. Layani, A. Kamyshny, S. Magdassi, Nanoscale 2014, **6**, 5581.
5   C. G. Granqvist, Sol. Energy Mater. Sol. Cells 2007, **91**, 1529.
6   M. G. Helander, Z. B. Wang, J. Qiu, M. T. Greiner, D. P. Puzzo, Z. W. Liu, Z. H. Lu, Science 2011, **332**, 944.
7   J. Cui, a. Wang, N. L. Edleman, J. Ni, P. Lee, N. R. Armstrong, T. J. Marks, Adv. Mater. 2001, **13**, 1476.
8   D. S. Hecht, L. Hu, G. Irvin, Adv. Mater. 2011, **23**, 1482.
9   R. G. Gordon, MRS Bull. 2000, **25**, 52.
10 L. Hu, D. S. Hecht, G. Gru, Chem. Rev., 2010, **110**, 5790.
11 A. A. Green, M. C. Hersam, Nano Lett. 2008, **8**, 1417.
12 M. W. Rowell, M. a. Topinka, M. D. McGehee, H. J. Prall, G. Dennler, N. S. Sariciftci, L. Hu, G. Gruner, Appl. Phys. Lett. 2006, **88**, 86.
13 D. Zhang, K. Ryu, X. Liu, E. Polikarpov, J. Ly, M. E. Tompson, C. Zhou, Nano Lett. 2006, **6**, 1880.
14 Z. Wu, Z. Chen, X. Du, J. M. Logan, J. Sippel, M. Nikolou, K. Kamaras, J. R. Reynolds, D. B. Tanner, A. F. Hebard, A. G. Rinzler, Science (80-.). 2004, **305**, 1273.
15 J. Y. Lee, S. T. Connor, Y. Cui, P. Peumans, Nano Lett. 2008, **8**, 689.
16 W. Gaynor, S. Hofmann, M. G. Christoforo, C. Sachse, S. Mehra, A. Salleo, M. D. McGehee, M. C. Gather, B. Lüssem, L. Müller-Meskamp, P. Peumans, K. Leo, Adv. Mater. 2013, **25**, 4006.
17 M. S. Miller, J. C. O'Kane, A. Niec, R. S. Carmichael, T. B. Carmichael, ACS Appl. Mater. Interfaces 2013, **5**, 10165.
18 A. Kim, Y. Won, K. Woo, S. Jeong, J. Moon, Adv. Funct. Mater. 2014, **24**, 2462.
19 M. Vosgueritchian, D. J. Lipomi, Z. Bao, Adv. Funct. Mater. 2012, **22**, 421.
20 M. Bolognesi, A. Sánchez-Díaz, J. Ajuria, R. Pacios, E. Palomares, Phys. Chem. Chem. Phys. 2011, **13**, 6105.
21 H. a. Becerril, J. Mao, Z. Liu, R. M. Stoltenberg, Z. Bao, Y. Chen, ACS Nano 2008, **2**, 463.

22 G. Eda, Y. Y. Lin, S. Miller, C. W. Chen, W. F. Su, M. Chhowalla, Appl. Phys. Lett. 2008, **92**, 10.

23 X. Li, G. Zhang, X. Bai, X. Sun, X. Wang, E. Wang, H. Dai, Nat Nano 2008, **3**, 538.

24 X. Wang, L. Zhi, K. Müllen, Nano Lett. 2008, **8**, 323.

25 W. Hong, Y. Xu, G. Lu, C. Li, G. Shi, Electrochem. Commun. 2008, **10**, 1555.

26 V. C. Tung, L.-M. Chen, M. J. Allen, J. K. Wassei, K. Nelson, R. B. Kaner, Y. Yang, Nano Lett. 2009, **9**, 1949.

27 J. Wu, M. Agrawal, a Becerril, Z. Bao, Z. Liu, Ḱ. Y. Chen, P. Peumans, ACS Nano, 2010, **4**, 43.

28 T. M. Barnes, M. O. Reese, J. D. Bergeson, B. A. Larsen, J. L. Blackburn, M. C. Beard, J. Bult, J. van de Lagemaat, Adv. Energy Mater. 2012, **2**, 353.

29 S. De, T. M. Higgins, P. E. Lyons, E. M. Doherty, P. N. Nirmalraj, W. J. Blau, J. J. Boland, J. N. Coleman, ACSNano 2009, **3**, 1767.

30 W. Gaynor, J. Y. Lee, P. Peumans, ACS Nano 2010, **4**, 30.

31 J. Robertson, J. Phys. C Solid State Phys. 1979, **12**, 4767.

32 M. Mäki-Jaskari, T. Rantala, Phys. Rev. B 2001, 64, 1.

33 R. J. Choudhary, S. B. Ogale, S. R. Shinde, V. N. Kulkarni, T. Venkatesan, K. S. Harshavardhan, M. Strikovski, B. Hannoyer, Appl. Phys. Lett. 2004, **84**, 1483.

34 C. G. Fonstad, R. H. Rediker, J. Appl. Phys. 1971, **42**, 2911.

35 Y. Huang, Q. Zhang, G. Li, M. Yang, Mater. Charact. 2009, **60**, 415.

36 Z. B. Zhou, R. Q. Cui, Q. J. Pang, Y. D. Wang, F. Y. Meng, T. T. Sun, Z. M. Ding, X. B. Yu, Appl. Surf. Sci. 2001, **172**, 245.

37 Y. Feng, R. Yao, L. Zhang, Mater. Chem. Phys. 2005, **89**, 312.

38 C. T. Wang, M. T. Chen, Mater. Lett. 2009, **63**, 389.

39 B. Zhang, Y. Tian, J. X. Zhang, W. Cai, Mater. Lett. 2011, **65**, 1204.

40 K. Ravichandran, P. Philominathan, J. Mater. Sci. Mater. Electron. 2011, **22**, 158.

41 K. C. Mishra, K. H. Johnson, P. C. Schmidt, Phys. Rev. B 1995, **51**, 13972.

42 J. Boltz, D. Koehl, M. Wuttig, Surf. Coatings Technol. 2010, **205**, 2455.

43 J. Huang, Y. Pan, J. Yuan, B. Yau, 2004, **184**, 188.

44 X. Xiao, G. Dong, J. Shao, H. He, Z. Fan, Appl. Surf. Sci. 2010, **256**, 1636.

45 H. Viirola, L. Niinistö, Thin Solid Films 1994, **251**, 127.

46 J. Kane, H. P. Schweizer, W. Kern, 1976, **123**, 270.

47 D. E. Carlson, J. Electrochem. Soc. 1975, **122**, 1334.

48 M. E. White, O. Bierwagen, M. Y. Tsai, J. S. Speck, J. Appl. Phys. 2009, **106**, 093704.

49 A. R. Babar, S. S. Shinde, a. V. Moholkar, C. H. Bhosale, J. H. Kim, K. Y. Rajpure, J. Alloys Compd. 2010, **505**, 416.

50 A. R. Babar, S. S. Shinde, a. V. Moholkar, C. H. Bhosale, J. H. Kim, K. Y. Rajpure, J. Alloys Compd. 2011, **509**, 3108.

51 D. Zhang, Z. Deng, J. Zhang, L. Chen, Mater. Chem. Phys. 2006, **98**, 353.

52 V. Müller, M. Rasp, G. Śtefanić, J. Ba, S. Günther, J. Rathousky, M. Niederberger, D. Fattakhova-Rohlfing, Chem. Mater. 2009, **21**, 5229.

53 L. Luo, D. Bozyigit, V. Wood, M. Niederberger, Chem. Mater. 2013, **25**, 4901.

54 V. Müller, M. Rasp, J. Rathouský, B. Schütz, M. Niederberger, D. Fattakhova-Rohlfing, Small 2010, **6**, 633.

55 M. Esro, G. Vourlias, C. Somerton, W. I. Milne, G. Adamopoulos, Adv. Funct. Mater. 2015, **25**, 134.

56 H. H. Chou, C. H. Cheng, Adv. Mater. 2010, 22, 2468.

57 M.-H. Tsai, H.-W. Lin, H.-C. Su, T.-H. Ke, C. -c. Wu, F.-C. Fang, Y.-L. Liao, K.-T. Wong, C.-I. Wu, Adv. Mater. 2006, 18, 1216.

58 B. L. Xiao, S. Su, Y. Agata, H. Lan, J. Kido, Adv. Mater. 2009, 21, 1271.

59 P. Desai, P. Shakya, T. Kreouzis, W. P. Gillin, J. Appl. Phys. 2007, 102, 073710.

60 J. S. Swensen, E. Polikarpov, A. Von Ruden, L. Wang, L. S. Sapochak, A. B. Padmaperuma, Adv. Funct. Mater. 2011, **21**, 3250.

61 J.-J. Lin, W-S. Liao, H-J. Huang, F.-L. Wu, C.-H. Cheng, Adv. Funct. Mater. 2008, **18**, 485.

62 J. Tauc, R. Grigorovici, A. Vancu, Phys. Status Solidi 1966, **15**, 627.

63 E. Burstein, Phys. Rev. 1954, **93**, 632.

64 E. Shanthi, V. Dutta, A. Banerjee, K. L. Chopra, J. Appl. Phys. 1980, **51**, 6243.

65 A. Rohatgi, T. R. Viverito, L. H. Slack, J. Am. Ceram. Soc. 1974, **57**, 278.

66 G. Haacke, J. Appl. Phys. 1976, **47**,622.

67 M. Kojima, H. Kato, M. Gatto, Philos. Mag. Part B 1993, **68**, 215.

68 H. Kim, C. M. Gilmore, J. S. Horwitz, a Pique, H. Murata, G. P. Kushto, R. Schlaf, Z. H. Kafafi, D. B. Chrisey, Appl. Phys. Lett. 2000, **76**, 259.

69 X. Zhou, J. He, L. S. Liao, M. Lu, Z. H. Xiong, X. M. Ding, X. Y. Hou, F. G. Tao, C. E. Zhou, S. T. Lee, Appl. Phys. Lett. 1999, **74**, 609.

70 A. Klein, C. Körber, a. Wachau, F. Säuberlich, Y. Gassenbauer, R. Schafranek, S. P. Harvey, T. O. Mason, Thin Solid Films 2009, **518**, 1197.

71 M. Batzill, U. Diebold, Prog. Surf. Sci. 2005, 79, 47.

72 D. F. Cox, T. B. Fryberger, S. Semancik, Phys. Rev. B 1988, **38**, 2072.

73 C. Körber, J. Suffner, a Klein, J. Phys. D. Appl. Phys. 2010, **43**, 055301.